Radiation-induced segregation on dislocation loops in austenitic Fe-Cr-Ni alloys

C. Dai [1,*] P. Saidi [2] B. Langelier [3] Q. Wang,[1] C. D. Judge,[4] M. R. Daymond [2] and M. Mattucci [1]

[1]*Canadian Nuclear Laboratories, Chalk River, Ontario K0J 1J0, Canada*
[2]*Department of Mechanical and Materials Engineering, Queen's University, Kingston, Ontario K7L 3N6, Canada*
[3]*Canadian Centre for Electron Microscopy, McMaster University, 1280 Main Street West, Hamilton, Ontario L8S 4L8, Canada*
[4]*Idaho National Laboratory, Idaho Falls, Idaho 83415, USA*

Radiation-induced segregation of alloying elements to crystallographic defects is commonly observed in irradiated austenitic stainless steels. The interaction between solutes and radiation-induced defects changes the physical distribution of solutes and thus affects the formation and growth of defects. The change of the microstructure consequently affects the mechanical properties of the material. A qualitative and quantitative understanding of the interaction between solutes and defects is desirable to better predict the service lifetime of nuclear materials. We used atom probe tomography to measure the distribution of solutes at dislocation loops in 304L stainless steel, irradiated with 2 MeV protons up to 1.5 displacements per atom at 373 and 633 K. No segregation at dislocation loops was found in samples irradiated at 373 K, whereas Ni and Si enrichment and Cr depletion were detected at dislocation loops irradiated at 633 K. The experimentally observed perfect and faulted dislocation loops in vacancy and interstitial types were reproduced by molecular dynamics (MD). A hybrid MD/Monte Carlo method was used to predict the redistribution of alloying atoms at all possible types of dislocation loops in face-centered cubic Fe-Cr-Ni alloys at the same irradiated temperatures (373 and 633 K). The simulations show that, at both temperatures, Cr clusters were formed and distributed randomly, and Ni atoms enriched or depleted at interstitial or vacancy dislocation loops, respectively. The change of solute concentration reaches the highest at the edge of the loop. Ni profiles exhibit characteristic behavior in terms of the stress field of the loops: tension inside of vacancy loops showing depletion of Ni atoms compared with compression inside of interstitial loops showing enrichment of Ni atoms. In addition, the stress field is reduced after solute redistribution. The absence of alloying segregation observed in experiments at a lower temperature (373 K) is explained by a rate theory model: Low-temperature irradiation requires significantly longer irradiation time to see the same amount of segregation as at high temperatures because of the extremely low diffusion of vacancies at low temperatures.

I. INTRODUCTION

The lifetime of structural materials such as austenitic stainless steels for nuclear energy systems is determined by their resistance to high-irradiation-damage, high-temperature, and corrosive environments. In general, irradiation induces defects in solid materials through the interaction between the atoms in the material and high-energy particles such as neutrons [1,2], protons [3,4], ions [5,6], and electrons [7,8]. Generally, radiation damage consists of four stages: collision, thermal spike, quenching, and annealing [9]. At the end of the quenching stage ($\sim$10 ps), metastable point defects or defect clusters, such as self-interstitial atoms (SIAs) and SIA clusters as well as vacancies and vacancy clusters, are formed. The movement of point defects and defect clusters results in extended defects such as dislocation loops [10] and voids [6], which are usually formed at the final stage of the damage event or built up over many cascade events. Experiments report perfect and Frank (or faulted) dislocation loops in austenitic steels

after irradiation at various temperatures [10,11]: the size and density of the Frank loops decrease and increase, respectively, with increasing irradiation temperature, whereas increasing irradiation dose correlates with increasing loop density. In addition, the density of Frank loops can be decreased at higher irradiation temperatures (823–873 K) by unfaulting to perfect loops [12]. Accumulation of radiation-induced defects can change the local microstructure, and the formation of these defects is further substantially influenced by the irradiation temperature [13,14]. Nonequilibrium mobile defects will tend to flow toward sinks, such as grain boundaries. This flux of defects leads to radiation-induced segregation (RIS) if a given alloying element has a preferential association with a specific defect type. Alloying elements segregate preferentially to defects (e.g., irradiation-induced dislocation loops) which act as obstacles to dislocation slip [15,16]. Therefore, a good understanding of the mechanisms related to RIS is essential in predicting and improving material service lifetime.

Two main mechanisms have been proposed to describe RIS: (1) the preferential exchange of solute atoms with the vacancy flux, so-called inverse-Kirkendall (IK) vacancy diffusion mechanism [17,18], and Eq. (2) the preferential

*Corresponding author: cong.dai@cnl.ca

association of undersized atoms with the interstitial flux, so-called interstitial drag mechanism [19,20]. Undersized solutes such as Ni and Si in Fe typically segregate to sinks, whereas oversized substitutional elements like Cr and Mo in Fe are depleted [21]. Allen *et al.* [22] suggest that the IK mechanism can reasonably reproduce the segregation behavior, but the interstitial drag mechanism cannot; the interstitial diffusivities were assumed equal for Cr, Fe, and Ni in their model. Stepanov *et al.* [23] reasonably reproduced the concentration profiles near grain boundaries from experiments at irradiation temperatures from 323 to 723 K by combining both the interstitial and vacancy mechanisms and including the binding energies of chemical elements with grain boundaries in their model. A CALPHAD-based model developed by Yang *et al.* [24] was used to analyze the diffusion fluxes near and at the grain boundaries of irradiated Fe-Cr-Ni alloys, and their results suggest that the dominant diffusion mechanism for Cr and Fe is via vacancies, whereas Ni can switch from the vacancy to the interstitial dominant mechanism. Authors of an *ab initio* modeling study [25] showed that both vacancies and interstitials contribute significantly to the RIS of Si atoms in Fe. In another study, Bruemmer *et al.* [26] suggest that the segregation of the undersized solute (Si) demonstrated the interstitial drag mechanism. RIS in alloys irradiated at low temperatures with electrons and ions [27,28] shows evidence of the interstitial mechanism of RIS as vacancies are practically immobile at the investigated temperatures of 25–50 °C. The temperature effect on RIS was measured and modeled in austenitic Fe-Cr-Ni alloys at temperatures between 200 and 600 °C, and the maximum Cr depletion (and Ni enrichment) occurs near 400 °C [22,29].

The solute segregation to dislocation loops can be pronounced, as reported by Kenik and Hojou [30] and Kenik [31], and the total dislocation density may also be influenced by RIS. This was further supported by Zinkle *et al.* [10], who observed that loop formation may be inhibited due to the modification of the chemical composition by RIS. Edwards *et al.* [32] found that RIS to Frank loops could alter their stability by changing their stacking fault energy (SFE). Lu *et al.* [33] measured the SFE of a set of 20 at.% Cr-austenitic stainless steels by transmission electron microscopy (TEM) and showed the same trend compared with values from first-principles calculations. It is worth noting that both alloying atoms and temperature could impact SFE. The alloying elements Ni and Cr have a positive effect on SFE from both experimental evidence [33] and first-principles calculations [34,35]. Molnár *et al.* [36] computed SFE of intrinsic and extrinsic stacking faults (SFs) in the {111} plane at temperatures from 298 to 773 K from first-principles calculations for 316L austenitic stainless steel, and the SFE of both SFs were increased as temperature increased.

Difficulties in working with irradiated materials and limitations in characterization techniques highlight the advantages of using atomistic simulations to help study RIS to defects. Wang *et al.* [37] used the molecular statics technique to investigate the stability of interstitial loops in a random alloying distribution system. The interaction between line dislocation and Frank loops was simulated by the molecular dynamics (MD) technique [38–40]; it was found that Frank loops are

strong obstacles and may unfault after interaction with a line dislocation. The effect of solute segregation to dislocation loops in austenitic stainless steels at the atomistic scale is still unknown.

In this paper, we combine atom probe tomography (APT) analysis, atomistic simulation, and rate theory modeling to study the solute distribution to four types of dislocation loops in austenitic stainless steels. The experimental measurement approach and computational methods are described in the next section. In the results section, the alloying distribution around observed proton-irradiated dislocation loops in 304L stainless steel is measured by APT. The interaction between solutes and all possible types of loops in austenitic Fe10Ni20Cr alloy is investigated by atomistic simulations. The alloying element distribution and stress fields are linked to explore the mechanisms driving solute segregation. The rate theory model qualitatively and quantitatively reproduces the experimental results, which give us the confidence to reasonably predict alloying segregation at longer times than are available using atomistic approaches. The results from different techniques are thoroughly discussed, and some critical conclusions are included to improve our understanding of RIS in austenitic stainless steels; the temperature of irradiation influences alloying element segregation to the irradiated induced dislocation loops, and hence, the properties of the loops themselves depend on the irradiation temperature under which they were formed.

II. METHODOLOGY

A. APT

Hot-rolled 304L stainless steel (0.019% C, 0.46% Si, 1.66% Mn, 18.19% Cr, 0.54% Mo, 0.38% Cu, 8.06% Ni, 0.129% Co, 0.032% P, 0.029% S, and 0.091% N) had been previously irradiated using a 2 MeV proton beam at 373 and 633 K up to 1.5 displacements per atom (dpa; measured at 60% of the damage peak depth), which was calculated using the Kinchin-Pease (K-P) algorithm in the Stopping and Range of Ions in Matter (SRIM) software as suggested by Stoller *et al.* [41]. The displacement threshold energy was set to 40 eV for iron-based alloys [41,42]. The dose rate for the proton irradiation was $\sim 10^{-5}$ dpa s^{-1}. The material specimen for APT was prepared using an FEI Versa dual-beam focused-ion beam scanning electron microscope (FIB-SEM) with a Ga ion source and extracted in plane view from the plateau region (depth of 5–15 μm) using standard *ex situ* lift-out methods and attached to presharpened Si posts [43]. Samples on the Si posts were sharpened into needles using annular FIB milling at 30 kV, with a final cleaning and sharpening step at 5 kV to reduce damage from the Ga ion beam. More details about the irradiation and specimen preparation can be found in our previous papers [44,45].

The APT acquisition was performed using a Cameca local electrode atom probe 4000X HR operating in laser-pulsing mode ($\lambda = 355$ nm, 40 pJ, and 200 kHz) with a target evaporation rate of 0.01 ions/pulse (1.0%) maintained by applying a DC voltage between 2 and 9 kV. The specimen stage was kept at a temperature of ~ 36 K, with an analysis chamber pressure of 2.5×10^{-11} Torr.

Data reconstruction and analysis were conducted using IVAS 3.8.2 and established reconstruction methods [46]. Spatial calibration was performed using SEM images of the tip shape before APT analysis and by checking against the measured plane spacings at identified crystal poles.

B. Hybrid MD/Monte Carlo method

The interatomic potential used in this paper to simulate dislocation loops in the face-centered cubic (fcc) structure of the FeNiCr alloy is that developed by Bonny *et al.* [35], which is a follow-up to their earlier work [47]. Comparing these two versions, the updated potential (EAM-13) [35] is more focused on the Fe10Ni20Cr alloy and has a better description of the SFEs. Alloying elements Ni and Cr were randomly introduced to the simulation box to form the Fe10Ni20Cr alloy. The total number of atoms is 1.44 million in the simulations, and the dimension of the simulation box is $25.2 \times 26.2 \times 24.7$ nm ($\langle 110 \rangle$, $\langle 11\bar{2} \rangle$, and $\langle 1\bar{1}\bar{1} \rangle$ directions). We used the same methodology described in Refs. [48–50] to create dislocation loops; their size is 12 nm in diameter (~2523 point defects for a perfect loop and ~2053 point defects for a Frank loop), which is comparable with experimental observations [25,32,44,45,51–53]. Vacancy-type Frank loops are studied in addition to the commonly investigated interstitial-type Frank loops, due to their observation in some previous experiments [11,32]. Perfect dislocation loops have Burgers vector $a/2 \langle 110 \rangle$ with a habit plane of {110}, and Frank dislocation loops have Burgers vector $a/3 \langle 111 \rangle$ with a habit plane of {111}.

After the creation of a single dislocation loop in four different simulation boxes for the four different types of loops described previously, all systems were initially relaxed at 373 or 633 K within the isobaric-isothermal ensemble for at least 500 ps. A hybrid MD/Monte Carlo (MC) method [54] was then used to simulate alloying element redistribution under thermal equilibrium. MD/MC simulations determine the thermodynamically correct occupation of atoms around dislocation loops but do not provide any information as to the kinetics of the diffusion process since that would require prohibitively long computational times. In this model, MC is applied for atomic movement together with MD to optimize the acceptance probability and provide better system relaxations to attain the minimal free energy. As a result, thermodynamically correct configurations of atomic sites can be determined. MC is an equilibrium simulation method that cannot be used to simulate nonequilibrium cascade conditions. However, the introduction of dislocation loops allows for the simulation of materials driven into a nonequilibrium state, where MC becomes useful to examine the phase stability and aging as materials move back toward equilibrium [55,56]. Due to the limits on computational availability, 2 million swap attempts (200 ps in MD) are provided for either Ni or Cr atoms to swap with Fe atoms.

Note that the experimentally observed dislocation loops are formed from the accumulation of irradiated point defects. In addition, the interaction between the loops and solute atoms evolves during the growth of the loops. The effect of the growth of the loops (involving the diffusion of point defects) cannot be considered in the current atomistic simulations due to long computational times, as discussed previously.

We note that mesoscale numerical approaches such as cluster dynamics and object kinetic MC are promising computational techniques to consider the diffusion of point defects during RIS but are outside the scope of this paper.

Atomistic simulations were performed using the Large-scale Atomic/Molecular Massively Parallel Simulator [57]. Periodic boundary conditions were applied to all directions in all simulations. Images of atomic configurations were produced with the Open Visualization Tool [58], and crystal structures are identified using common neighbor analysis (CNA) [59] and the dislocation extraction algorithm [60].

C. Rate theory model

To quantify the temperature effect on RIS in austenitic stainless steels, we adopted a rate theory model developed in Refs. [19,61,62] that connects the rates of defect generation, migration, and recombination in the vicinity of an ideal sink. The defect kinetic process in a quaternary system (Fe20Cr8Ni1Si) is determined by coupling five independent nonlinear partial differential equations (PDEs):

$$\frac{\partial c_{i/v}}{\partial t} = G - \nabla \cdot J_{i/v} - R_{i,v}c_i c_v, \tag{1}$$

$$\frac{\partial c_k}{\partial t} = -\nabla \cdot J_k, \tag{2}$$

where $c_{i/v}$ represents the concentration of interstitials/vacancies, G is the Frenkel pair production rate, and c_k is the concentration of elements Fe, Ni, Cr, and Si. The recombination coefficient $R_{i,v}$ is determined by the following equation [63]:

$$R_{i,v} = \frac{4\pi r_{i,v}}{\Omega} \sum_{k=\text{Fe,Ni,Cr,Si}} (d_{k,v} + d_{k,i})c_k, \tag{3}$$

where $r_{i,v}$ is the recombination radius, and Ω is the average atomic volume. Here, $d_{k,v}$ (or $d_{k,i}$) is the kinetic coefficient of element k via vacancy (or interstitial) movement:

$$d_{k,v/i} = \frac{1}{6}z_{v/i}f_{k,v/i}\lambda_{v/i}^2\omega_{k,v/i}^0 \exp\left(-\frac{E_{k,v/i}^m}{k_B T}\right), \tag{4}$$

where $z_{v/i}$ is the number of nearest neighbours, $f_{k,v/i}$ is the correlation factor, $\lambda_{v/i}$ is the jump distance, $\omega_{kv/i}$ is the pre-exponential factor, $E_{k,v/i}^m$ is the migration energy, k_B is Boltzmann's constant, and T is the absolute temperature. The flux of point defects ($J_{i/v}$) and alloying elements (J_k) are determined from the following framework of RIS theory [9]:

$$J_{i/v} = \pm\alpha c_{i/v} \sum_{k=\text{Fe,Ni,Cr,Si}} (d_{k,i/v}\nabla c_k)$$
$$- \nabla c_{i/v} \sum_{k=\text{Fe,Ni,Cr,Si}} (d_{k,i/v}c_k), \tag{5}$$

$$J_k = -\alpha\nabla c_k \sum_{d=i,v} (d_{k,d}c_d) + c_k(d_{k,v}\nabla c_v - d_{k,i}\nabla c_i). \tag{6}$$

The $\pm$ in Eq. (5) represents the scenario for the flux of vacancies and interstitials, respectively. The thermodynamic parameter α accounts for the difference between the chemical potential gradient and the concentration gradient, which is

assumed as unity. Si atoms are first assumed to be on the same sublattice as Fe, Cr, and Ni. An alternative approach is to consider Si atoms in a separate sublattice. In this latter case, the flux of Si atoms is independent of other components. Therefore, the change of concentration over the course of irradiation is calculated as $\frac{\partial c_{\mathrm{Si}}}{\partial t} = D_{\mathrm{Si,i}} \nabla^2 c_{\mathrm{si,i}}$, where $D_{\mathrm{Si,i}}$ is the diffusivity of Si via its corresponding sublattice.

It should be noted that the presence of solute atoms in the interstitial sites is affected by the binding of solute atoms to interstitials due to atomic size mismatch. Interstitials tend to bind to undersize atoms, such as Si, and consequently, the sinks become enriched with Si. To account for solute-interstitial binding in the diffusivity coefficients, we need to know the interstitial binding energy ($E_{k,i}^{\mathrm{b}}$), which is the average energy gained by converting the type of interstitial atoms to atom type k. For instance, ($E_{\mathrm{Si,i}}^{\mathrm{b}}$) is the average energy gained for converting Fe, Cr, or Ni interstitials to an Si interstitial. In our system, Si is the most prone to occupying the interstitial site and segregate due to its negative volume misfit and strong binding to interstitials [64,65]. However, the thermodynamic parameters required for accurate simulation, such as $E_{k,i}^{\mathrm{b}}$ in the system in this paper is not available in the literature and must be estimated. Therefore, we acknowledge that the probability of presence of a specific atom type in the interstitial site is not equal to the concentration, and this will introduce uncertainty into the results. To indirectly include the effect of preferentially binding the interstitials to Si, the pre-exponential factor ($\omega_{\mathrm{Si,i/v}}^0$) and migration energy of Si ($E_{\mathrm{Si,v}}^{\mathrm{m}}$) are treated as fitting parameters under the condition that $\frac{d_{\mathrm{Si,v}}}{d_{k,v}} - \frac{d_{\mathrm{Si,i}}}{d_{k,i}} < 0$, where k is other elements of the system (Fe, Ni, or Cr). Satisfying this condition guarantees that Si that binds to interstitials will undergo enrichment at sinks by virtue of the flow of interstitials to the sink [9].

Two irradiation temperatures (373 and 633 K) were considered, and the initial material is assumed to be annealed with negligible grain interior sink strength due to dislocations. The initial concentrations of interstitials and vacancies are the equilibrium values based on the method specified in Ref. [62]. The initial condition for alloying elements is a uniform distribution according to the composition of the alloy.

Two parallel ideal sinks (grain boundary and dislocation loop) are considered at a distance of 1.5 μm, and the coupled PDEs of Eqs. (1) and (2) are solved for the domain in between. The distance is sufficient to avoid overlap of the sink effect from sinks that are located at the two ends of the domain. The boundary conditions are as follows: the concentration of point defects remains unchanged and equal to the equilibrium concentration, and the flux of alloying elements at each end is zero. The input parameters used for model calculations are listed in Table I.

The irradiated systems are forced out of equilibrium. Far-from-equilibrium conditions lead to rich and complex behaviors in both kinetics and mechanisms of diffusion. Diffusion coefficients used in this paper (i.e., in Ref. [29]) were computed from the defect formation energies that assume equilibrium concentrations. However, under irradiation, the concentration of defects is not near equilibrium. This approximation to the equilibrium condition (neglecting the interaction between defects) would introduce uncertainties to the results.

TABLE I. List of the input parameters used for the rate theory model.

Input parameters		Value and references
Recombination radius	$r_{\mathrm{i,v}}$	1×10^{-9} m [64]
Pre-exponential factors	$\omega_{\mathrm{Fe,v}}^0$	1.6×10^{13} s^{-1} [29]
	$\omega_{\mathrm{Cr,v}}^0$	2.4×10^{13} s^{-1} [29]
	$\omega_{\mathrm{Ni,v}}^0$	1.0×10^{13} s^{-1} [29]
	$\omega_{\mathrm{Si,v}}^0$	1.6×10^{13} s^{-1} (fitted)
	$\omega_{\mathrm{Fe/Cr/Ni,i}}^0$	1.5×10^{12} s^{-1} [29]
	$\omega_{\mathrm{Si,i}}^0$	0.9×10^{11} s^{-1} (fitted)
Correlation factors	f_{v}	1 [29]
	f_{i}	0.44 [29]
Migration energies	$E_{\mathrm{Fe,v}}^{\mathrm{m}}$	1.21 eV [29]
	$E_{\mathrm{Cr,v}}^{\mathrm{m}}$	1.21 eV [29]
	$E_{\mathrm{Ni,v}}^{\mathrm{m}}$	1.197 eV [29]
	$E_{\mathrm{Si,v}}^{\mathrm{m}}$	1.16 eV (fitted)
	$E_{\mathrm{Fe/Cr/Ni,i}}^{\mathrm{m}}$	0.9 eV [29]
	$E_{\mathrm{Si,i}}^{\mathrm{m}}$	0.83 eV [66]
Entropy of vacancy formation	$S_{\mathrm{v}}^{\mathrm{f}}$	$1k_{\mathrm{B}}$ [62]
Formation energy of Fe vacancy	$E_{\mathrm{Fe,v}}^{\mathrm{f}}$	1.6 eV [67]
Formation energy of Fe interstitial	$E_{\mathrm{Fe,i}}^{\mathrm{f}}$	5 eV [29]

III. RESULTS

A. Distribution of solutes for dislocation loops by APT analysis

Dislocation loops irradiated to 1.5 dpa at 373 K have smaller loop size ($\sim$7 nm in diameter) but higher loop density ($\sim$ 3.2–3.5 m^{-3}) than those at 633 K ($\sim$12 nm and 1.0–2.3 m^{-3}), which was reported in our recent TEM work [44,45]. The experiments in this paper use the same materials but focus on the solute segregation at dislocation loops at 373 and 633 K. As illustrated in Fig. 1(a) (with 4.5 at. % Si isosurfaces, 0.5 nm cubic voxels, and 2.5 nm delocalization), we found little to no segregation in samples irradiated at 373 K, whereas visible segregation was identified in samples irradiated at 633 K [see Fig. 1(b)]. An individual loop is isolated as shown in Fig. 1(c), and the visualization of the loop is aided by generating isoconcentration surfaces for Si, such as shown in Fig. 1(d). To measure a radial profile from the center of the loop, a cylindrical region of interest (ROI) is located coaxially with the loop. For the data shown in Fig. 1(e), the thickness of the loop (i.e., the dimension along the Z cylindrical axis of the ROI) was set to 4 nm, as that was the apparent width of the Si isoconcentration surface along that dimension. As the loop was not a perfect circle, the cross-section of the ROI was set to match its elliptical shape, with a ratio of major to minor axes (R/r) of 1.16. Concentrations were measured by binning atoms within cylindrical shells at set minor radii increments of 0.25 nm, with the results plotted in Fig. 1(f). Clear maxima of Ni and Si (and corresponding minima of Fe and Cr) appear at $\sim$4.25 nm. The concentration profiles gradually change with distance, reaching constant values at 7–9 nm, and it appears that the segregation distance is 2–4 nm. The concentrations inside and outside the loop appear approximately identical.
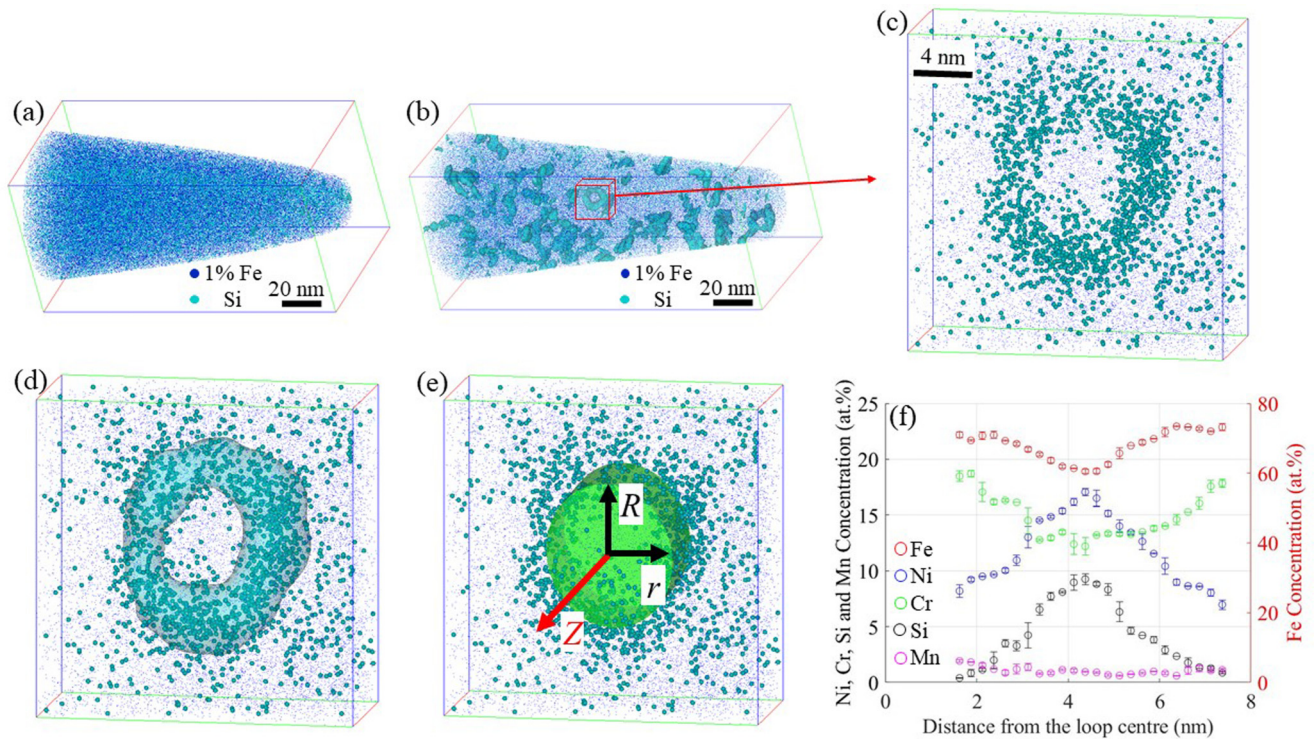
FIG. 1. Atom probe tomography (APT) analysis of proton-irradiated 304L stainless steel with 2 MeV protons (~1.5 dpa) at (a) 373 K and (b) 633 K with isosurfaces for 4.5 at. % Si reveal segregation regions, and a marked region indicates a single dislocation loop that is isolated in (c). (d) 3 at. % Si isosurface to position the region of interest (ROI). (e) Cylindrical ROI with 4 nm thickness. (f) Elemental concentration from the ROI.

B. Motivation for atomistic simulations

The solute redistribution around the dislocation loop has been experimentally observed in other austenitic stainless steels. RIS to the dislocation loops was detected by energy dispersive x-ray spectroscopy (EDS) in the ion irradiation experiment of Kenik (316 stainless steel at 790 and 950 K) [31] and the neutron irradiation experiment of Kenik and Hojou (304 stainless steel at 561 K) [30], and their results show Cr depletion and Ni enrichment at the dislocation loops that are suggested to be Frank loops. Using APT on ion-irradiated 316 stainless steel at 623 K, Etienne *et al.* [51] observed segregation of Ni and Si and depletion of Cr at rounded and torus-shaped clusters, which are also believed to be Frank loops. For proton-irradiated 304 stainless steel at 633 K, Jiao and Was [4] found the enrichment of Si, Ni, and P and the depletion of Cr and Mn at the edge of the loop using APT and scanning TEM-EDS.

Very few experiments focus on solute redistribution for austenitic steels irradiated at temperatures <473 K (the lowest irradiation temperature reported above is 561 K [30], yet this of practical interest since 473 K is a representative temperature of the CANDU calandria vessel operating condition [45]). Furthermore, there appears to be little to no segregation in samples irradiated at 373 K in this paper and our previous work [44,45]. Although TEM can be used to identify the types of loops present in a sample [44,45], it can be a challenge to unambiguously determine which type of loop is present in the subsequently examined APT sample due to a lack of specific crystallographic information. In atomistic simulations,

different types of dislocation loops can be constructed based on the experimentally measured information (the Burgers vector, the habit plane of the loop, and vacancy or interstitial type). Therefore, atomistic simulations will be helpful to predict possible segregation behaviors at different types of loops at various temperatures.

C. Alloying redistribution for all possible types of dislocation loops by atomistic simulations

The simulation box was sliced to a 1-nm-thick (~3 times the lattice parameter) sampling volume that envelops a loop to better present the alloying redistribution around dislocation loops. The thickness direction is along the normal direction of the plane of the loop. The strain energy (the subtraction of the potential energy of the selected system from the potential energy in a perfect crystal for the same type of atoms) and the concentration map of each element are presented on the projection of the plane of the loop, and they are illustrated in Figs 2 and 3 for temperatures of 373 and 633 K, respectively. Note that the diameter of the loop is ~12 nm for all types of loops, comparable with that seen experimentally at 633 K. The atomic configurations (with only displaced atoms) of dislocation loops are illustrated to compare with the alloying distribution. Displaced atoms inside the Frank loops are due to the existence of SFs.

Ni and Cr atoms are randomly distributed before the alloying redistribution (as imposed during setup), and there is then an obvious redistribution of the solute atoms after the MD/MC simulation steps (see Figs 2 and 3). Cr atoms are likely to form
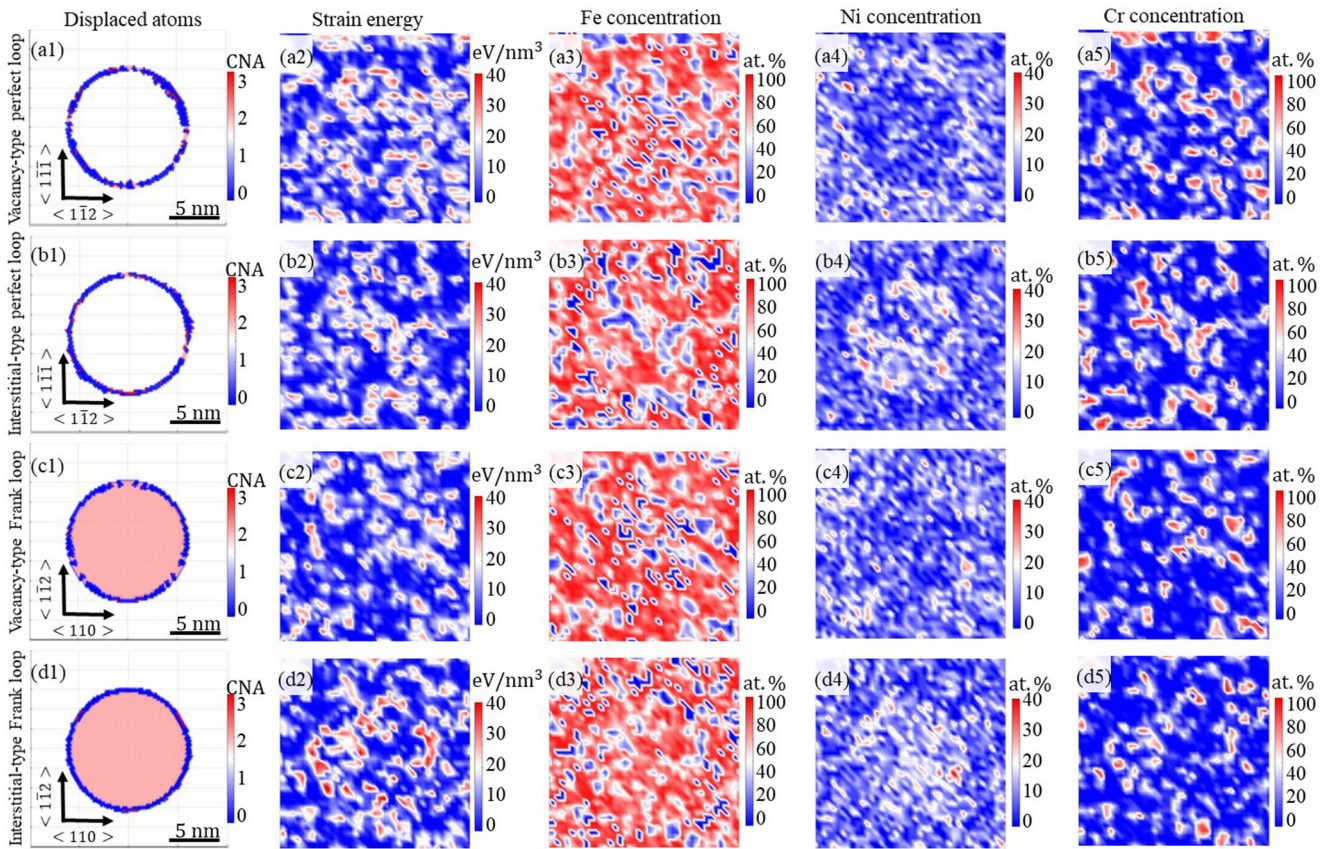
FIG. 2. Measured at 373 K. (1)–(5) are displaced atoms colored by common neighbor analysis (CNA), strain energy map, and concentration map of Fe/Ni/Cr for (a) vacancy-type perfect loop, (b) interstitial-type perfect loop, (c) vacancy-type Frank loop, and (d) interstitial-type Frank loop.

local clusters randomly. These Cr clusters are not identified as displaced atoms according to the structural analysis in this paper, as they are still in the fcc structure. The existence of Cr clusters was reported by Shankar *et al.* [68] in austenitic stainless steels using TEM and x-ray diffraction. They found that these Cr clusters were formed during the early stages of aging at 1123 K and had the same fcc structure as the parent austenite.

Ni redistribution seems to be correlated to the configuration of dislocation loops, and it is also related to the types of loops: There is Ni depletion inside the vacancy loops of both perfect and Frank types and Ni enrichment inside interstitial loops of both perfect and Frank types. As noted, the simulations were performed at two different temperatures (373 and 633 K), and Ni depletion and enrichment as well as Cr clusters are observed in both cases, as shown in Figs 2 and 3. To explore the redistribution of solute atoms, the concentration and strain energy distribution are discretized in a series of shells at increasing distances from the loop center, and their profiles are shown in Fig. 4. Inside the vacancy loops ($\leqslant 6$ nm), the Ni amount is generally $<10\%$, and it is $>10\%$ at regions outside ($\geqslant 6$ nm) of the vacancy loops; it shows a reverse behavior for the interstitial loops. Furthermore, Ni concentration mostly shows a significant difference at regions close to the edge of the loops (~ 6 nm). Moreover, Ni concentration reaches its equilibrium concentration (10%) when

it is ~ 10 nm away from the loop center. This suggests that the redistribution of Ni atoms around dislocation loops is confined to short-range distances from the loop, which is consistent with previous experiments [26,53]. Therefore, the segregation distance induced by Ni redistribution outside of the loop is estimated as 2–4 nm in this paper. The effect of loop size on the segregation distance of Ni is not significant, and a smaller loop (4-nm-diameter loop) has a similar segregation distance.

The APT results illustrated in Fig. 1(f) show Ni enrichment inside the dislocation loop, although the type of this specific loop cannot be determined due to lack of crystallographic information. Although previous experimental studies [30,31,51] hypothesized that loops presenting Ni enrichment are likely Frank loops, a sound explanation is still needed. The current atomistic simulations predict that both interstitial-type perfect and Frank loops exhibit Ni enrichment inside the dislocation loop. In addition, both perfect and Frank loops were experimentally detected on the same samples in our previous work [44,45]. Therefore, the extracted dislocation loop shown in Fig. 1(b) could be either an interstitial-type perfect or an interstitial-type Frank loop.

High strain energy locations in the strain energy map are likely correlated with locations of high Cr concentration, as shown in Figs 2 and 3. Moreover, as illustrated in Fig. 4, low and high Cr positions are usually associated with low and high
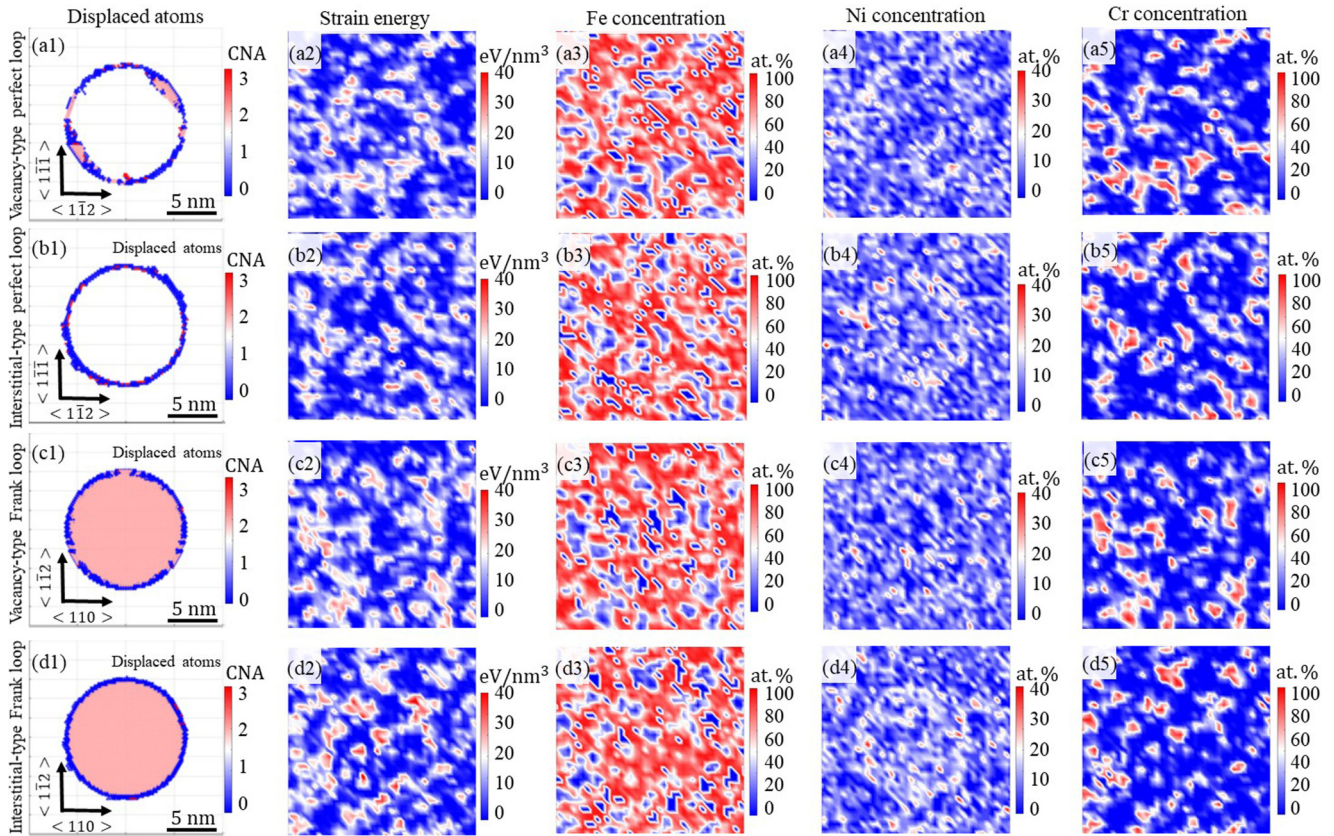
FIG. 3. Measured at 633 K. (1)–(5) are displaced atoms colored by common neighbor analysis (CNA), strain energy map, and concentration map of Fe/Ni/Cr for (a) vacancy-type perfect loop, (b) interstitial-type perfect loop, (c) vacancy-type Frank loop, and (d) interstitial-type Frank loop.

strain energies, respectively. Additionally, the strain energy always exhibits a peak at the edge of the loops (∼6 nm), where atoms are significantly displaced.

D. Stress field analysis by atomistic simulations

The radial component of the stress of each atom [69] is converted from Cartesian coordinates to cylindrical
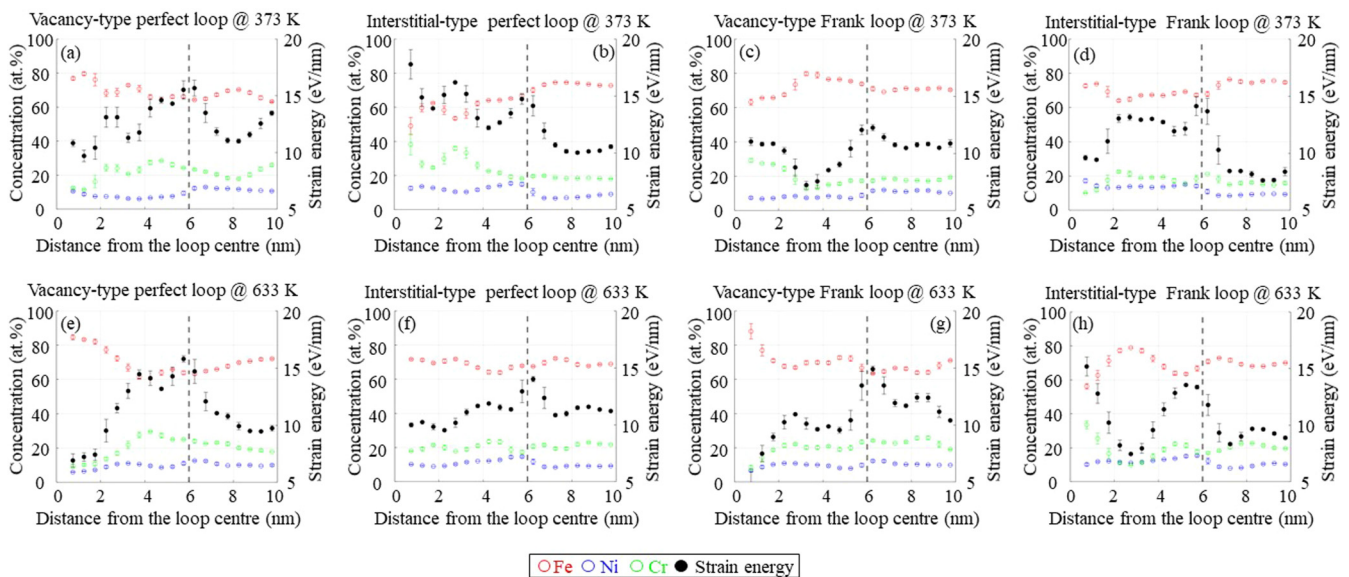
FIG. 4. The concentration profile of each element and the strain energy as a function of the distance from the loop center for (a) and (e) vacancy-type perfect loops, (b) and (f) interstitial-type perfect loops, (c) and (g) vacancy-type Frank loops, and (d) and (h) interstitial-type Frank loops. (a)–(d) are measured at 373 K, and (e)–(h) are measured at 633 K. The loop edge is highlighted by a black dashed line at 6 nm.
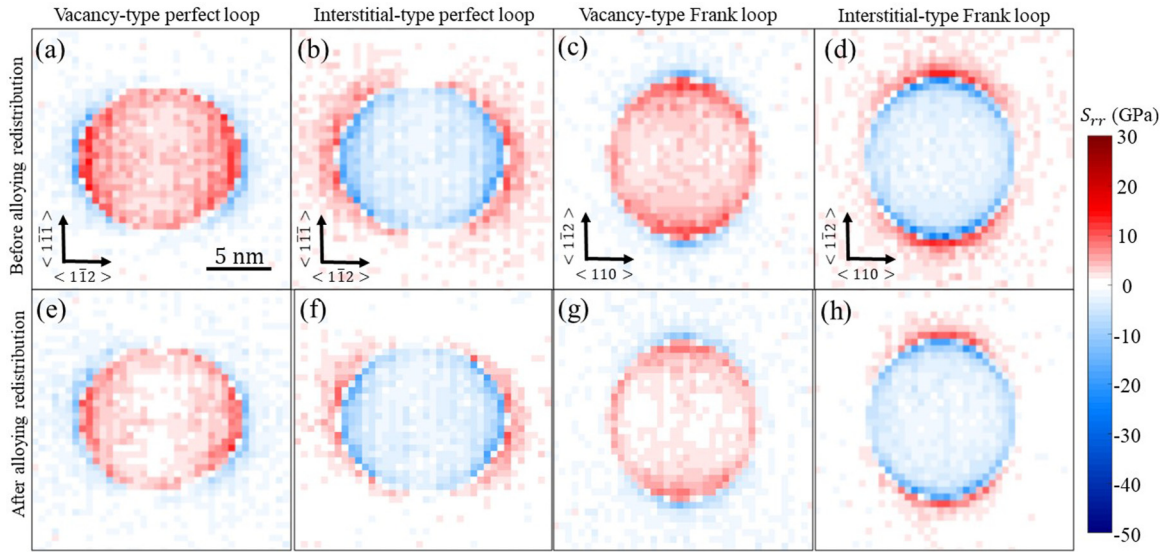
FIG. 5. After annealing at 373 K, under the condition of (a)–(d) no alloying segregation and (e)–(h) with alloying segregation: the radial stress component of stress (S_{rr}) for (a) and (e) a vacancy-type perfect loop, (b) and (f) an interstitial-type perfect loop, (c) and (g) a vacancy-type Frank loop, and (d) and (h) an interstitial Frank loop.

coordinates to better represent the stress field around a dislocation loop due to its geometry [56]. Positive and negative stresses are tensile and compressive, respectively. Using this method, we present the stress state in cylindrical coordinates on the projection of the plane of the loop. In Fig. 5 (373 K) and Fig. 6 (633 K), the radial component of stress (S_{rr}) is used to describe the stress field around all types of dislocation loops in this paper before and after alloying redistribution. Vacancy loops present tension inside the loop, whereas interstitial loops exhibit compression, which is due to the absence of atoms for vacancy loops and the presence of excess atoms for interstitial loops. Stress is concentrated at the edge of all loops, which is consistent with the strain energy field calcu-

lated previously (Figs 2 and 3). Moreover, the stress shows the highest contrast along the $\langle 1\bar{1}2 \rangle$ direction. This is due to the shortest bonds between atoms along the $\langle 1\bar{1}2 \rangle$ direction ($\sim$0.73 Å), whereas the bonding distances along the directions $\langle 110 \rangle$ and $\langle 1\bar{1}\bar{1} \rangle$ are $\sim$1.26 and $\sim$2.06 Å, respectively. Therefore, S_{rr} is maximized at the edge of the loop along the $\langle 1\bar{1}2 \rangle$ direction.

The stress decreases for all loops at both temperatures after alloying redistribution, as shown in Figs 5 and 6. In our earlier study [56], we also suggest Ni segregation to dislocation loops in hexagonal close-packed Zr can decrease the stress around loops. The previous results showed Ni depletion for vacancy loops and Ni enrichment for interstitial loops, especially at the
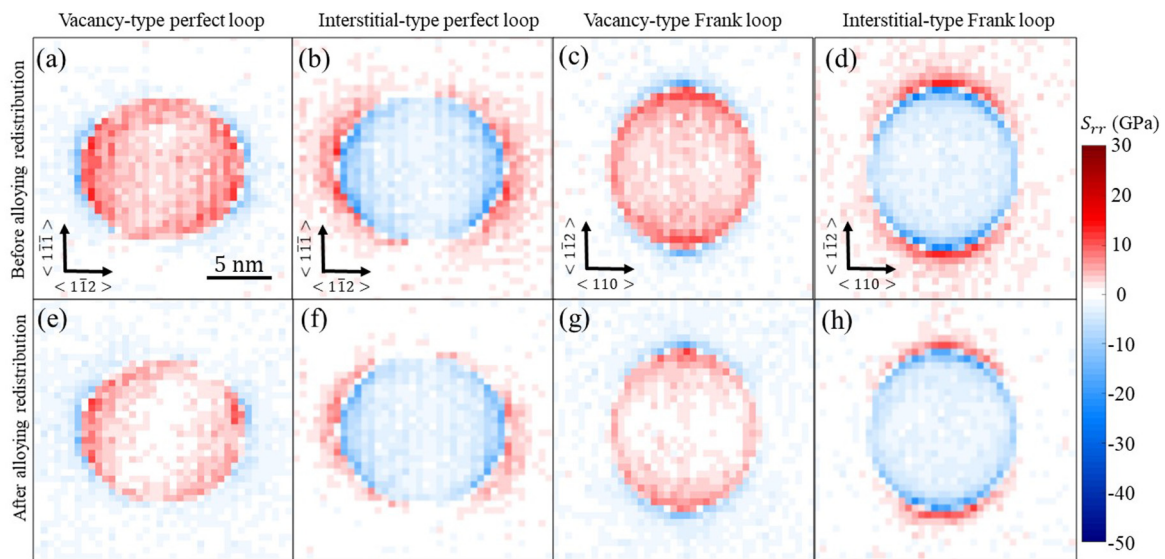

FIG. 6. After annealing at 633 K, under the condition of (a)–(d) no alloying segregation and (e)–(h) with alloying segregation: the radial stress component of stress (S_{rr}) for (a) and (e) a vacancy-type perfect loop, (b) and (f) an interstitial-type perfect loop, (c) and (g) a vacancy-type Frank loop, and (d) and (h) an interstitial Frank loop.
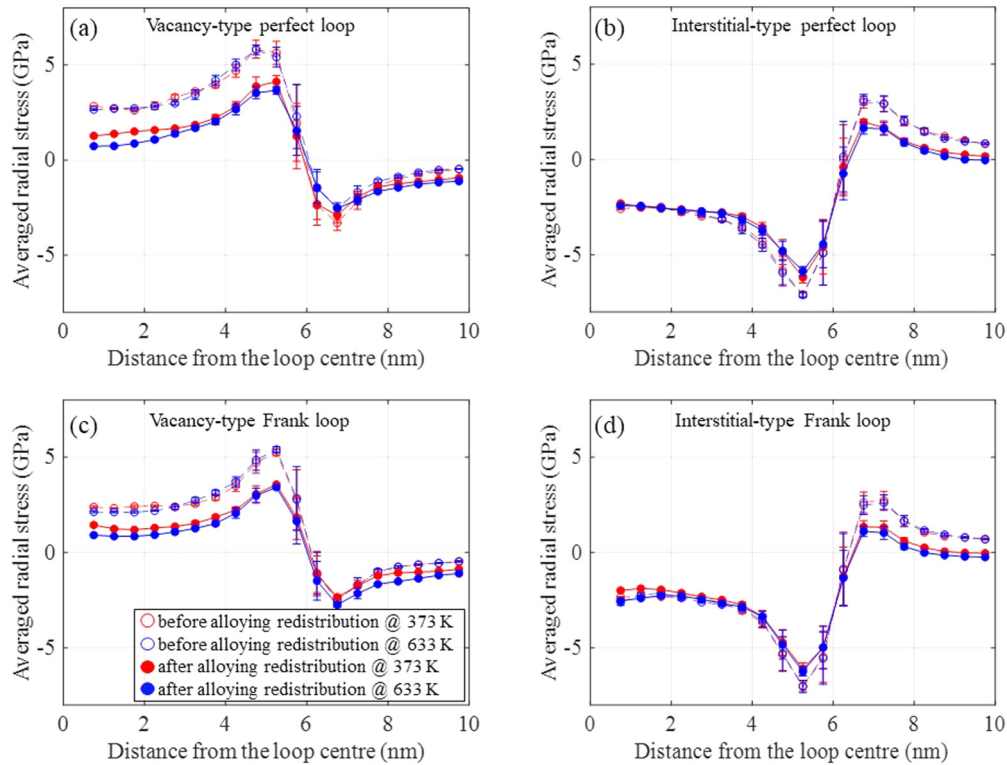
FIG. 7. The averaged radial stress component (S_{rr}) after annealing at 373 K (red data) and 633 K (blue data), under the condition of no alloying segregation (open circles) and with alloying segregation (closed circles): (a) vacancy-type perfect loops, (b) interstitial-type perfect loops, (c) vacancy-type Frank loops, and (d) interstitial-type Frank loops. The loop edge is at 6 nm.

edge of the loops. A comparison between the Ni concentration map [Figs 2(c) and 3(c)] and the stress field map (Figs 5 and 6) suggests that Ni depletion (enrichment) for vacancy (interstitial) loops is responsible for stress reduction. Ni atoms may prefer to segregate to compressive locations to release tension due to the smaller atomic size of Ni atoms [27,28,70].

The radial stress was averaged within cylindrical shells as a function of distance from the loop center (like the concentration profiles above), as shown in Fig. 7. All the stress profiles exhibit a significant contrast at the loop edge (6 nm). For the case of vacancy loops, the stress gradually increases from the loop center and reaches a maximum at 5 nm, which is 1 nm away from the loop edge, and then drops quickly to a minimum at 6.5 nm, which is 0.5 nm away from the loop edge. For the case of interstitial loops, the stress gradually decreases from the loop center and reaches a minimum at 5.5 nm, which is 0.5 nm away from the loop edge, and then increases quickly to a maximum at 7 nm, which is 1 nm away from the loop edge. For both vacancy and interstitial loops, the averaged radial stress at the loop edge (6 nm) and locations outside of the loop (>9 nm) are ∼0. The averaged stresses before alloying redistribution (open circles) are generally higher than those after alloying redistribution (closed circles), and particularly for the region of tensile behavior (positive stress). More precisely, for the change of the stress field of vacancy loops [see Figs. 7(a) and 7(c)], the stress decreases inside the loop until the edge of the loop, and then the stress remains relatively stable beyond that region. For the change of the stress field of interstitial loops [see Figs. 7(b) and 7(d)], the stress inside the loop is stable from 0 to 4 nm

and then becomes less negative until the edge of the loop. The stress also decreases outside of interstitial loops and becomes negligible at 10 nm from the loop center. The stress at the edge of both vacancy and interstitial loops remains unchanged after the alloying redistribution.

According to these simulations, the temperature effect is not significant for interstitial-type perfect loops and both interstitial and vacancy-type Frank loops, but there is a noticeable difference at the edge of the loop for vacancy-type perfect loops, i.e., Fig. 7(a). The stress field at the edge of vacancy-type perfect dislocation loops at a lower temperature (373 K) is relatively higher than that at a higher temperature (633 K). In our previous work [50], we show that dislocation dissociation is increased as temperature increases for vacancy-type perfect loops. These dissociated dislocations would form SFs at the edge of vacancy-type perfect loops, which may decrease the stress field. It is also interesting to note that the alloying redistribution does not affect the locations of the stress maximum or minimum.

The Ni concentration profiles have an approximately inverse relationship with the stress profiles, which is illustrated in Fig. 8. The locations (along the distance from the loop center) of the stress at the maximum (minimum) generally correspond to Ni concentration at the minimum (maximum). This observation further indicates the correlation between the redistribution of Ni atoms and the stress distribution. Ni atoms are depleted inside vacancy loops, and the tension is thus decreased. As described previously, the stress becomes less compressive at locations near the edge of the interstitial loop after alloying redistribution. Ni concentration profiles in
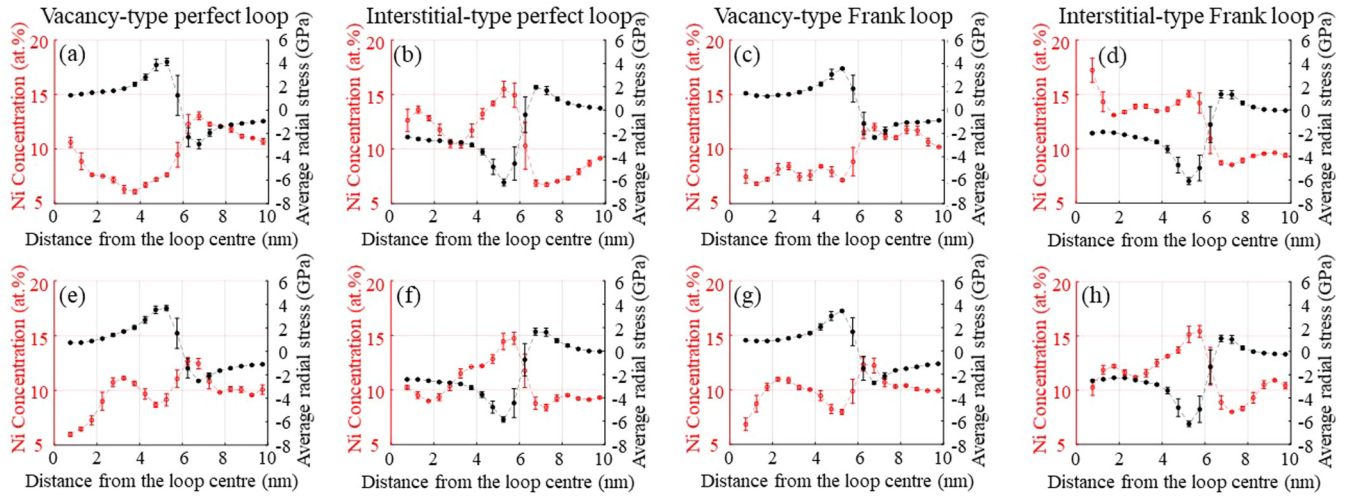
FIG. 8. After alloying redistribution, Ni concentration (red) and the averaged radial stress (black) as a function of the distance from the loop center for (a) and (e) a vacancy-type perfect loop, (b) and (f) an interstitial-type perfect loop, (c) and (g) a vacancy-type Frank loop, and (d) and (h) an interstitial-type Frank loop. (a)–(d) are measured at 373 K, and (e)–(h) are measured at 633 K. The loop edge is at 6 nm.

Figs. 8(b), 8(d), 8(f), and 8(h) for interstitial loops show that Ni accumulation starts to gradually increase at ∼4 nm, which is consistent with the change of the stress field analyzed previously.

E. RIS analysis by a rate theory model

As noted above, the atomistic simulations suggest that—thermodynamically—segregation is expected at both irradiation temperatures. However, this is not observed experimentally; rather segregation is only seen experimentally for

the high-temperature irradiation. While we can qualitatively assign this to kinetic effects, to explore this difference quantitatively, we need modeling which can describe the kinetics of alloying element segregation. Figure 9 shows comparisons between the prediction of the rate theory model (1.5 dpa at an irradiation rate of 10^{-5} dpa s^{-1}) and APT data at 373 and 633 K. Note that the APT data for the loop start from the edge of the loop. At 373 K, APT data of high-angle grain boundaries (purple squares) show a small Cr and Si enrichment at grain boundaries, and Ni segregation is negligible. At 633 K, APT data of RIS in the vicinity of sinks
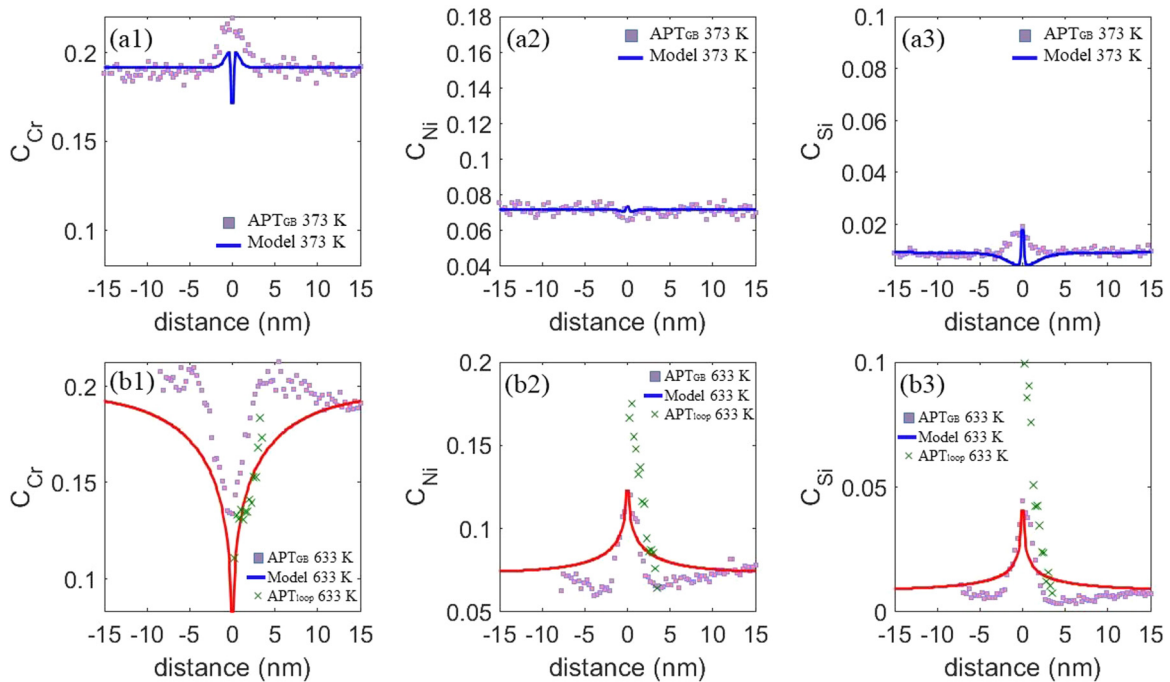

FIG. 9. The representative concentration profiles of (a) Cr, (b) Ni, and (c) Si across an ideal sink at 373 K (upper) and 633 K (bottom) based on the prediction of the model (1.5 dpa at an irradiation rate of 10^{-5} dpa s^{-1}). Purple square and green cross markers represent atom probe tomography (APT) measurements for grain boundaries [45,72] and the dislocation loop, respectively.
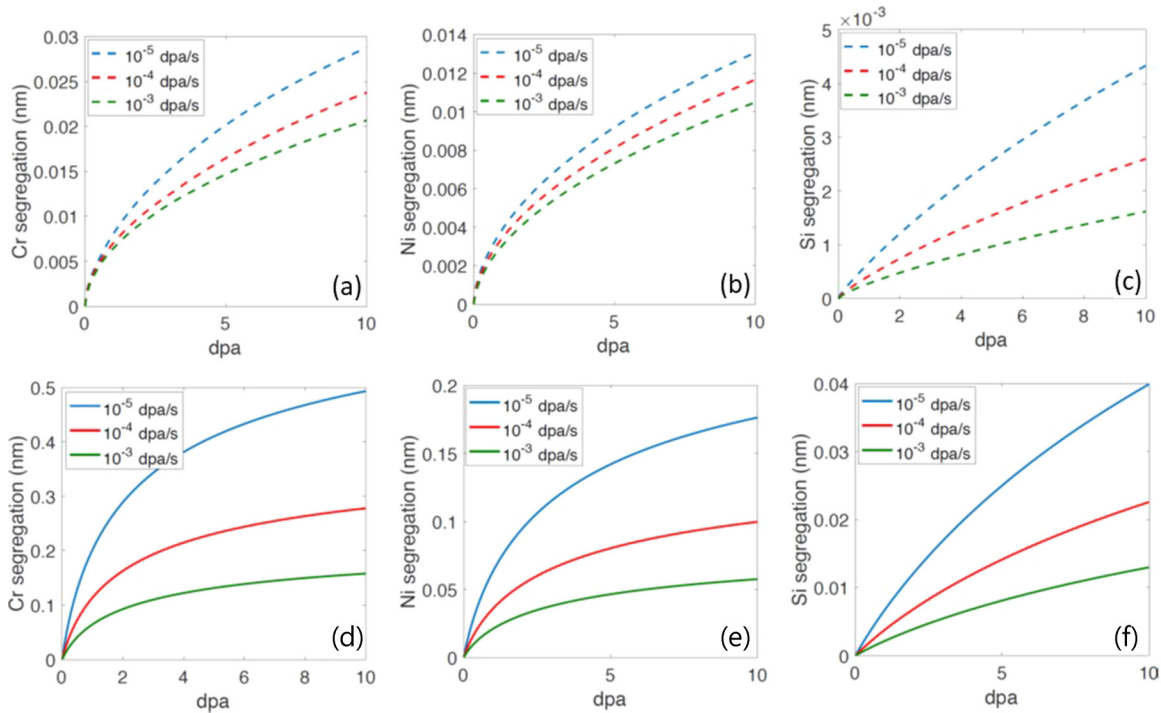
FIG. 10. Total segregation of the representative concentration as a function of irradiation damage at (a)–(c) 373 K and (d)–(f) 633 K at three irradiation rates: 10^{-5}, 10^{-4}, and 10^{-3} dpa s^{-1}.

(both grain boundary and vacancy loop) show Cr depletion and Ni and Si enrichment, which also agrees with previous studies [29,71]. There is a slight increase (decrease) for the Cr (Ni) and Si profiles approaching the sinks. These slight changes of solute concentration are not captured by the continuum model at this high temperature, but they are observed at a lower temperature by the model in Figs 9(a1), 9(b1), and 9(c1).

Relatively faster diffusion of Cr than Ni via vacancies ($d_{Cr,v}/d_{Ni,v} = 1.89$ at 633 K) results in Cr depletion and Ni enrichment at the grain boundaries, which is based on the IK vacancy diffusion mechanism [17,18]. The Si enrichment at the grain boundaries is explained by the interstitial drag mechanism [19,20]: undersized elements (such as Si) are preferentially bound to interstitials to segregate at grain boundaries. As the redistribution of Cr and Ni is driven by the IK vacancy diffusion mechanism, their negligible segregation at 373 K predicted by the rate theory model can be explained by the extremely low diffusion of vacancies at low temperatures.

The alloying segregation at low temperatures (i.e., 373 K) is negligible according to the APT analysis as well as the rate theory model in this paper. While a significant alloying redistribution, especially for Ni, was found at 373 K in our MD/MC simulations, it is important to note that the description of the diffusion process is limited in MD/MC; alloying atoms find their thermodynamically correct locations, as previously discussed, without true consideration of the kinetics. The energy barrier due to the migration energy of point defects at low temperatures may prohibit alloying redistribution; however, it should be noted that higher irradiation damage could promote additional alloying segregation.

The samples studied in the APT analysis and the rate theory model previously were irradiated up to 1.5 dpa. The influence of increased irradiation damage can be investigated by increasing irradiation time and/or irradiation rate in the model. Here, we used the rate theory model to compare alloying segregation with three different irradiation rates (10^{-5}, 10^{-4}, and 10^{-3} dpa s^{-1}) at 373 and 633 K up to 10 dpa. Total segregation (c_{seg}^k) is defined to represent the deviation of the concentration profile [$c(x)$] from the nominal concentration (c_0^k):

$$c_{seg}^k = \int_{-L}^{L} \frac{\left| c(x) - c_0^k \right|}{2} dx, \qquad (7)$$

where L is equal to half of the domain length, as illustrated in Fig. 9. The total segregation of all elements increases as a function of irradiation damage at both temperatures (see Fig. 10). Moreover, at the condition of the same irradiation damage, the total segregation increases when the irradiation rate (temperature) decreases (increases). At the same irradiation rate condition, a much longer irradiation time is needed for low-temperature irradiation to reach the same segregation than high-temperature irradiation. For example, for the irradiation rate of 10^{-5} dpa s^{-1}, the corresponding irradiation damage for the total segregation of Ni of 0.01 nm is 0.086 dpa when irradiated at 633 K [see Fig. 10(f)], whereas the corresponding irradiation damage is 5.9 dpa at 373 K [see Fig. 10(b)]. Therefore, the segregation decreases significantly at low temperatures. This calculation explains the negligible segregation observed at low temperatures in the APT analysis; at such temperatures, significantly longer irradiation times will be required to see the same amount of segregation as at high temperatures.

IV. DISCUSSIONS

A. Alloying redistribution and stress field of dislocation loops

Solute segregation to dislocation loops has been experimentally observed in the literature [30–32] and the APT analysis conducted in this paper. A decrease of the Gibbs free energy of the system is the driving force for solute segregation to defects [73]. Solute redistribution can change the stress field of dislocation loops. The atomistic simulations in this paper show that the stress field around loops decreases after the redistribution of solute atoms, and Ni distribution has a strong relationship with the stress field. Ni atoms are undersized atoms compared with Fe and Cr atoms, and undersized atoms are expected to segregate to the compressive regions [74,75]. The effect of chemical segregation on the structure of dislocations was recently reported in a Pt-Au model alloy [76]. A key conclusion of their study [76] is that the chemical nature of dislocations is strongly linked to their underlying structure and associated distortion fields. Therefore, the stress field analysis in this paper provides an important understanding of the chemical nature of dislocations.

The correlation between the stress field and solute profiles (particularly for Ni) is magnified at the region close to the edge of the loop based on the MD/MC simulations. Ni concentration outside of the loop but still near the edge of the loop shows a slight increase (decrease), which is opposite to the depletion (enrichment) of Ni concentration inside the loop (see Fig. 8). This feature is also observed by APT data at grain boundaries at a higher temperature (633 K) and is the prediction by the rate theory model at a lower temperature (373 K).

It should be noted that Ni redistribution is not the only factor that contributes to the change of the stress field of loops. As shown in Figs 7 and 8, although the depletion of Ni atoms is correlated to a decrease of tensile field, Ni enrichment has little effect on the compressive stress. In addition, the formation of Cr clusters after solute redistribution is related to local changes of strain energy, as evidenced in Fig. 4, which may influence the stress field.

B. Temperature effect on alloying redistribution

The diffusion of alloying elements and point defects is greatly affected by the change of temperature. Ni segregation was found in MD/MC simulations at both low and high temperatures, but experiments only found Ni segregation at high temperatures. The radiation can drive the system to nonequilibrium at relatively low irradiation temperature [77], whereas the MD/MC simulation can relax the system to more equilibrated status. The segregation predicted by the rate theory model suggests that the combination of irradiation time, flux, and temperature is key in determining the degree of alloying segregation. Low-temperature segregation requires a much longer time to reach the same segregation as at high temperatures, for a given flux. Solute segregation in an fcc metal foil was modeled and studied as a function of irradiation temperature, and the calculations show that solute segregation is significantly influenced by the irradiation temperature at temperatures below $\sim 0.5 T_m$ [78,79]. The factor of the irradiation time was considered in an analytical model proposed by Faulkner *et al.* [80] at given irradiation temperatures to

describe the grain boundary segregation. However, the irradiation time is not considered in the MD/MC model since the diffusion process is difficult to simulate, and the alloying redistribution is based only on thermodynamically correct occupations of atomic sites.

In addition, temperature could change the relative sink strength, which would then influence alloying redistribution; this is not considered in our rate theory model so far. First-principles calculations [34–36] found that the SFE of Frank dislocation loops increases with temperature. Higher SFE means dislocation loops are more difficult to generate but generally leads to greater loop mobility [81]. Frank loops in austenitic stainless steels are generally regarded as sessile [10,82,83], and the temperature effect on their sink strength is presently not fully understood. A recent modeling study by Jiang *et al.* [84] calculated the grain boundary sink strength of fcc Cu without considering the grain boundary stress effect, and they found that the grain boundary sink strength decreases as temperature increases.

Many previous studies [25,52,85–88] have sought to correlate irradiation-induced defects (such as Frank loops) on subsequent mechanical properties. It is to be expected [39,40,89] that the presence of alloying element segregation will influence the interaction between slip dislocations and the irradiation-induced defects, e.g., the barrier strength of the defects to slip. Our results demonstrate that the temperature of irradiation must be considered when determining barrier strengths; specifically, a loop will present a different barrier depending on the irradiation temperature under which it was formed due to the different associated alloying segregation.

V. CONCLUSIONS

In this paper, we have examined the effects of different types of dislocation loops, stress fields, and temperature on RIS in austenitic stainless steels. Our results show the correlation between the microchemical changes from segregation and the corresponding strain and stress field. Alloying depletion and enrichment to the dislocation loop was experimentally observed by APT. The correlation between the stress field of loops and the alloying redistribution was carefully elucidated by atomistic simulations. An APT informed rate theory model accurately predicted the alloying redistribution with different irradiation dose rates and temperatures. The results demonstrate the importance of considering the irradiation temperature under which defects were produced when determining the impact on mechanical properties. To fully characterize irradiation-induced defects, both the crystallographic and microchemical properties need to be understood. In conclusion:

(i) APT analysis shows little to no segregation at loops in samples irradiated at 373 K, whereas visible segregation (enrichment of Ni and Si and depletion of Fe and Cr) to the loop was identified in samples irradiated at 633 K, and the segregation distance is estimated as 2–4 nm.

(ii) MD/MC simulations found different alloying redistribution (particularly for the Ni element) for interstitial and vacancy loops: Ni depletion (enrichment) inside the vacancy (interstitial) loops but Ni enrichment (depletion) outside the vacancy (interstitial) loops. Moreover, the segregation distance is consistent with the APT results.

(iii) The stress field of loops reduces after alloying redistribution according to MD/MC simulations. In addition, a significant Ni concentration contrast near the edge of loops is found to correlate with the stress profiles.

(iv) The rate theory model can reasonably reproduce the APT data. With the same irradiation damage, higher irradiation rates may decrease the amount of segregation, as the irradiation time at higher irradiation rates is shorter than that at lower irradiation rates.

(v) High-temperature irradiation can lead to more alloying segregation than low-temperature irradiation, based on both experiments and the rate theory model.

[1] K. G. Field, Y. Yang, T. R. Allen, and J. T. Busby, Defect sink characteristics of specific grain boundary types in 304 stainless steels under high dose neutron environments, Acta Mater. **89**, 438 (2015).

[2] X. Zhang, C. Xu, Y. Chen, W. Y. Chen, J. S. Park, P. Kenesei, J. Almer, J. Burns, Y. Wu, and M. Li, High-energy synchrotron x-ray study of deformation-induced martensitic transformation in a neutron-irradiated type 316 stainless steel, Acta Mater. **200**, 315 (2020).

[3] Z. W. Zhang, C. T. Liu, X. L. Wang, M. K. Miller, D. Ma, G. Chen, J. R. Williams, and B. A. Chin, Effects of proton irradiation on nanocluster precipitation in ferritic steel containing fcc alloying additions, Acta Mater. **60**, 3034 (2012).

[4] Z. Jiao and G. S. Was, Segregation behavior in proton- and heavy-ion-irradiated ferritic-martensitic alloys, Acta Mater. **59**, 4467 (2011).

[5] M. A. Tunes, G. Greaves, T. M. Kremmer, V. M. Vishnyakov, P. D. Edmondson, S. E. Donnelly, S. Pogatscher, and C. G. Schön, Thermodynamics of an austenitic stainless steel (AISI-348) under *in situ* TEM heavy ion irradiation, Acta Mater. **179**, 360 (2019).

[6] S. Taller and G. S. Was, Understanding bubble and void nucleation in dual ion irradiated T91 steel using single parameter experiments, Acta Mater. **198**, 47 (2020).

[7] N. Sakaguchi, S. Watanabe, and H. Takahashi, Heterogeneous dislocation formation and solute redistribution near grain boundaries in austenitic stainless steel under electron irradiation, Acta Mater. **49**, 1129 (2001).

[8] Z. Yang and S. Watanabe, Dislocation loop formation under various irradiations of laser and/or electron beams, Acta Mater. **61**, 2966 (2013).

[9] G. S. Was, *Fundamentals of Radiation Materials Science: Metals and Alloys*, 2nd Ed. (Springer, New York, 2016).

[10] S. J. Zinkle, P. J. Maziasz, and R. E. Stoller, Dose dependence of the microstructural evolution in neutron-irradiated austenitic stainless steel, J. Nucl. Mater. **206**, 266 (1993).

[11] M. Desormeaux, B. Rouxel, A. T. Motta, M. Kirk, C. Bisor, Y. De Carlan, and A. Legris, Development of radiation damage during *in-situ* Kr++ irradiation of Fe-Ni-Cr model austenitic steels, J. Nucl. Mater. **475**, 156 (2016).

[12] W. Van Renterghem, M. J. Konstantinović, and M. Vankeerberghen, Evolution of the radiation-induced defect structure in 316 type stainless steel after post-irradiation annealing, J. Nucl. Mater. **452**, 158 (2014).

[13] C. C. Fu, J. D. Torre, F. Willaime, J. L. Bocquet, and A. Barbu, Multiscale modelling of defect kinetics in irradiated iron, Nat. Mater. **4**, 68 (2005).

[14] D. A. Terentyev, Y. N. Osetsky, and D. J. Bacon, Effects of temperature on structure and mobility of the ⟨100⟩ edge dislocation in body-centred cubic iron, Acta Mater. **58**, 2477 (2010).

[15] A. J. Jacobs and G. P. Wozadlo, Irradiation-assisted stress corrosion cracking as a factor in nuclear power plant aging, J. Mater. Eng. **9**, 345 (1988).

[16] G. S. Was, Y. Ashida, and P. L. Andresen, Irradiation-assisted stress corrosion cracking, Corros. Rev. **29**, 7 (2011).

[17] A. D. Marwick, R. C. Piller, and M. E. Horton, *Radiation-Induced Segregation in Fe-Cr-Ni Alloys* (British Nuclear Energy Society, United Kingdom, 1984).

[18] J. Perks, A. Marwick, and C. English, *Computer code to calculate radiation induced segregation in concentrated ternary alloys*, Report AERE-R-12121 (International Atomic Energy Agency, Vienna, 1986).

[19] H. Wiedersich, P. R. Okamoto, and N. Q. Lam, A theory of radiation-induced segregation in concentrated alloys, J. Nucl. Mater. **83**, 98 (1979).

[20] H. R. Brager and J. S. Perrin, Effects of radiation on materials, *21st International Symposium* (ASTM International, West Conshohocken, PA, 2004).

[21] C. M. Shepherd, Radiation-induced segregation in ion-irradiated stainless steels—the origin of compositional fluctuations in irradiated alloys, J. Nucl. Mater. **175**, 170 (1990).

[22] T. R. Allen, J. T. Busby, G. S. Was, and E. A. Kenik, On the mechanism of radiation-induced segregation in austenitic Fe-Cr-Ni alloys, J. Nucl. Mater. **255**, 44 (1998).

[23] I. A. Stepanov, V. A. Pechenkin, and Yu. V. Konobeev, Modeling of radiation-unduced segregation at grain boundaries in Fe-Cr-Ni alloys, J. Nucl. Mater. **329–333**, 1214 (2004).

[24] Y. Yang, K. G. Field, T. R. Allen, and J. T. Busby, Roles of vacancy/interstitial diffusion and segregation in the microchemistry at grain boundaries of irradiated Fe-Cr-Ni alloys, J. Nucl. Mater. **473**, 35 (2016).

[25] L. Tan, R. E. Stoller, K. G. Field, Y. Yang, H. Nam, D. Morgan, B. D. Wirth, M. N. Gussev, and J. T. Busby, Microstructural evolution of type 304 and 316 stainless steels under neutron irradiation at LWR relevant conditions, JOM **68**, 517 (2016).

[26] S. M. Bruemmer, E. P. Simonen, P. M. Scott, P. L. Andresen, G. S. Was, and J. L. Nelson, Radiation-induced material

changes and susceptibility to intergranular failure of light-water-reactor core internals, J. Nucl. Mater. **274**, 299 (1999).

[27] S. Watanabe, N. Sakaguchi, K. Kurome, M. Nakamura, and H. Takahashi, On the mechanism of radiation-induced segregation, J. Nucl. Mater. **240**, 251 (1997).

[28] G. V. Lysova, G. A. Birzhevoy, and N. I. Khramushin, The investigation of the mechanism of the radiation-induced segregation of elements near the surface of the Fe-20Cr-20Ni alloy after irradiation with iron ions, Surf. Investig. X-Ray, Synchrotron Neutron Tech. **16**, 787 (2001).

[29] T. R. Allen and G. S. Was, Modeling radiation-induced segregation in austenitic Fe-Cr-Ni alloys, Acta Mater. **46**, 3679 (1998).

[30] E. A. Kenik and K. Hojou, Radiation-induced segregation in FFTF-irradiated austenitic stainless steels, J. Nucl. Mater. **191–194**, 1331 (1992).

[31] E. A. Kenik, Radiation-induced solute segregation in a low swelling 316 stainless steel, Scr. Metall. **10**, 733 (1976).

[32] D. J. Edwards, E. P. Simonen, and S. M. Bruemmer, Evolution of fine-scale defects in stainless steels neutron-irradiated at 275 °C, J. Nucl. Mater. **317**, 13 (2003).

[33] J. Lu, L. Hultman, E. Holmström, K. H. Antonsson, M. Grehk, W. Li, L. Vitos, and A. Golpayegani, Stacking fault energies in austenitic stainless steels, Acta Mater. **111**, 39 (2016).

[34] C. Varvenne, A. Luque, W. G. Nöhring, and W. A. Curtin, Average-atom interatomic potential for random alloys, Phys. Rev. B **93**, 104201 (2016).

[35] G. Bonny, N. Castin, and D. Terentyev, Interatomic potential for studying ageing under irradiation in stainless steels: the FeNiCr model alloy, Model. Simul. Mater. Sci. Eng. **21**, 085004 (2013).

[36] D. Molnár, X. Sun, S. Lu, W. Li, G. Engberg, and L. Vitos, Effect of temperature on the stacking fault energy and deformation behaviour in 316L austenitic stainless steel, Mater. Sci. Eng. A **759**, 490 (2019).

[37] X. X. Wang, L. L. Niu, and S. Wang, Energetics analysis of interstitial loops in single-phase concentrated solid-solution alloys, J. Nucl. Mater. **501**, 94 (2018).

[38] J. B. Baudouin, A. Nomoto, M. Perez, G. Monnet, and C. Domain, Molecular dynamics investigation of the interaction of an edge dislocation with Frank loops in Fe-Ni$_{10}$-Cr$_{20}$ alloy, J. Nucl. Mater. **465**, 301 (2015).

[39] J. Hesterberg, R. Smith, and G. S. Was, Atomistic simulation of the obstacle strengths of radiation-induced defects in an Fe-Ni-Cr austenitic stainless steel, Model. Simul. Mater. Sci. Eng. **27**, 085004 (2019).

[40] D. Terentyev and A. Bakaev, Interaction of a screw dislocation with Frank loops in Fe-10Ni-20Cr Alloy, J. Nucl. Mater. **442**, 208 (2013).

[41] R. E. Stoller, M. B. Toloczko, G. S. Was, A. G. Certain, S. Dwarakanath, and F. A. Garner, On the use of SRIM for computing radiation damage exposure, Nucl. Instrum. Methods. Phys. Res. B **310**, 75 (2013).

[42] M. S. Wechsler, C. Lin, W. F. Sommer, L. U. L. Daemen, and P. D. Feguson, *ASTM E521-16: Standard Practice for Investigating the Effects of Neutron Radiation Damage Using Charged-Particle Irradiation* (ASTM International, West Conshohocken, 2009).

[43] K. Thompson, D. Lawrence, D. J. Larson, J. D. Olson, T. F. Kelly, and B. Gorman, *In situ* site-specific specimen preparation for atom probe tomography, Ultramicroscopy **107**, 131 (2007).

[44] M. A. Mattucci, Q. Wang, T. Skippon, M. R. Daymond, G. S. Was, J. Smith, and C. D. Judge, Nano-mechanical testing of proton irradiated 304L SS at 100 °C and 360 °C to support IASCC, in *19th International Conference on Environmental Degradation of Materials in Nuclear Power Systems—Water Reactors* (American Nuclear Society, Boston, 2019), pp. 1311–1321.

[45] C. D. Judge, B. Langelier, M. A. Mattucci, Q. Wang, M. Daymond, G. S. Was, and J. Smith, Microstructural characterization of proton irradiated 304L SS at 100 °C and 360 °C, in *19th International Conference on Environmental Degradation of Materials in Nuclear Power Systems—Water Reactors* (American Nuclear Society, Boston, 2019), pp. 513–522.

[46] B. Gault, M. P. Moody, J. M. Cairney, and S. P. Ringer, *Atom Probe Microscopy* (Springer Science & Business Media, New York, 2012), Vol. 160.

[47] G. Bonny, D. Terentyev, R. C. Pasianot, S. Poncé, and A. Bakaev, Interatomic potential to study plasticity in stainless steels: the FeNiCr model alloy, Model. Simul. Mater. Sci. Eng. **19**, 085008 (2011).

[48] C. Varvenne, O. Mackain, and E. Clouet, Vacancy clustering in zirconium: an atomic-scale study, Acta Mater. **78**, 65 (2014).

[49] E. Clouet, BABEL package, version 10.2, http://emmanuel. clouet.free.fr/Programs/Babel/index.html.

[50] C. Dai, Q. Wang, P. Saidi, B. Langelier, C. D. Judge, M. R. Daymond, and M. A. Mattucci, Atomistic structure and thermal stability of dislocation loops, stacking fault tetrahedra, and voids in face-centered cubic Fe, J. Nucl. Mater. **563**, 153636 (2022).

[51] A. Etienne, M. Hernández-Mayoral, C. Genevois, B. Radiguet, and P. Pareige, Dislocation loop evolution under ion irradiation in austenitic stainless steels, J. Nucl. Mater. **400**, 56 (2010).

[52] H. H. Jin, E. Ko, S. Lim, J. Kwon, and C. Shin, Effect of irradiation temperature on microstructural changes in self-ion irradiated austenitic stainless steel, J. Nucl. Mater. **493**, 239 (2017).

[53] Z. Jiao, J. Michalicka, and G. S. Was, Self-ion emulation of high dose neutron irradiated microstructure in stainless steels, J. Nucl. Mater. **501**, 312 (2018).

[54] B. Sadigh, P. Erhart, A. Stukowski, A. Caro, E. Martinez, and L. Zepeda-Ruiz, Scalable parallel Monte Carlo algorithm for atomistic simulations of precipitation in alloys, Phys. Rev. B **85**, 184203 (2012).

[55] K. Nordlund, Historical review of computer simulation of radiation effects in materials, J. Nucl. Mater. **520**, 273 (2019).

[56] C. Dai, P. Saidi, Z. Yao, and M. R. Daymond, Atomistic simulations of Ni segregation to irradiation induced dislocation loops in Zr-Ni alloys, Acta Mater. **140**, 56 (2017).

[57] S. Plimpton, Fast parallel algorithms for short-range molecular dynamics, J. Comput. Phys. **117**, 1 (1995).

[58] A. Stukowski, Visualization and analysis of atomistic simulation data with OVITO—the Open Visualization Tool, Model. Simul. Mater. Sci. Eng. **18**, 15012 (2010).

[59] D. Faken and H. Jónsson, Systematic analysis of local atomic structure combined with 3D computer graphics, Comput. Mater. Sci. **2**, 279 (1994).

[60] A. Stukowski and K. Albe, Extracting dislocations and non-dislocation crystal defects from atomistic simulation data, Model. Simul. Mater. Sci. Eng. **18**, 085001 (2010).

[61] M. Nastar and G. Martin, Modelling nonequilibrium grain boundary segregations, Mater. Sci. Forum **294–296**, 83 (1999).

[62] R. V. Skorokhod and A. V. Koropov, Modeling of radiation-induced segregation in Fe-Cr-Ni alloys, Phys. Solid State **61**, 2269 (2019).

[63] F. Soisson, Kinetic Monte Carlo simulations of radiation induced segregation and precipitation, J. Nucl. Mater. **349**, 235 (2006).

[64] P. R. Okamoto and H. Wiedersich, Segregation of alloying elements to free surfaces during irradiation, J. Nucl. Mater. **53**, 336 (1974).

[65] L. K. Mansur and M. H. Yoo, The effects of impurity trapping on irradiation-induced swelling and creep, J. Nucl. Mater. **74**, 228 (1978).

[66] X. Wang, H. Zhang, T. Baba, H. Jiang, C. Liu, Y. Guan, O. Elleuch, T. Kuech, D. Morgan, J. C. Idrobo, P. M. Voyles, and I. Szlufarska, Radiation-induced segregation in a ceramic, Nat. Mater. **19**, 992 (2020).

[67] P. Olsson, C. Domain, and J. Wallenius, *Ab initio* study of Cr interactions with point defects in bcc Fe, Phys. Rev. B **75**, 014110 (2007).

[68] P. Shankar, D. Sundararaman, and S. Ranganathan, Clustering and ordering of nitrogen in nuclear grade 316LN austenitic stainless steel, J. Nucl. Mater. **254**, 1 (1998).

[69] A. P. Thompson, S. J. Plimpton, and W. Mattson, General formulation of pressure and stress tensor for arbitrary many-body interaction potentials under periodic boundary conditions, J. Chem. Phys. **131**, 154107 (2009).

[70] M. Winter, WebElements the periodic table on the WWW, http://www.webelements.com/.

[71] H. Takahashi, N. Hashimoto, and S. Watanabe, Defect-flow-induced grain boundary migration with segregation under electron irradiation, Ultramicroscopy **56**, 193 (1994).

[72] M. A. Mattucci, Q. Wang, B. Langelier, C. Dai, M. Daymond, N. Huin, and C. D. Judge, Examining the effects of irradiation temperature on defect generation and the nature of dislocation loops, arXiv:2203.02403 (2022).

[73] G. Da Rosa, P. Maugis, J. Drillet, V. Hebert, and K. Hoummada, Co-segregation of boron and carbon atoms at dislocations in steel, J. Alloys Compd. **724**, 1143 (2017).

[74] V. Kuksenko, C. Pareige, C. Genevois, and P. Pareige, Characterisation of Cr, Si and P distribution at dislocations and grain-boundaries in neutron irradiated Fe-Cr model alloys of low purity, J. Nucl. Mater. **434**, 49 (2013).

[75] V. Kuksenko, C. Pareige, and P. Pareige, Intra granular precipitation and grain boundary segregation under neutron irradiation in a low purity Fe-Cr based alloy, J. Nucl. Mater. **425**, 125 (2012).

[76] X. Zhou, J. R. Mianroodi, A. K. Da Silva, T. Koenig, G. B. Thompson, P. Shanthraj, D. Ponge, B. Gault, B. Svendsen, and D. Raabe, The hidden structure dependence of the chemical life of dislocations, Sci. Adv. **7**, eabf0563 (2021).

[77] G. S. Was, J. P. Wharry, B. Frisbie, B. D. Wirth, D. Morgan, J. D. Tucker, and T. R. Allen, Assessment of radiation-induced segregation mechanisms in austenitic and ferritic-martensitic alloys, J. Nucl. Mater. **411**, 41 (2011).

[78] R. A. Johnson and N. Q. Lam, Solute segregation under irradiation, J. Nucl. Mater. **69–70**, 424 (1978).

[79] R. A. Johnson and N. Q. Lam, Solute segregation to voids during irradiation, Phys. Rev. B **15**, 1794 (1977).

[80] R. G. Faulkner, S. Song, P. E. J. Flewitt, M. Victoria, and P. Marmy, Grain boundary segregation under neutron irradiation in dilute alloys, J. Nucl. Mater. **255**, 189 (1998).

[81] A. Kelly and K. M. Knowles, *Crystallography and Crystal Defects*, 2nd Ed. (John Wiley & Sons, Hoboken, 2012).

[82] J. J. Holmes, R. E. Robbins, J. L. Brimhall, and B. Mastel, Elevated temperature irradiation hardening in austenitic stainless steel, Acta Metall. **16**, 955 (1968).

[83] H. R. Brager and J. L. Straalsund, Defect development in neutron irradiated type 316 stainless steel, J. Nucl. Mater. **46**, 134 (1973).

[84] C. Jiang, N. Swaminathan, J. Deng, D. Morgan, and I. Szlufarska, Effect of grain boundary stresses on sink strength, Mater. Res. Lett. **2**, 100 (2014).

[85] G. E. Lucas, The evolution of mechanical property change in irradiated austenitic stainless steels, J. Nucl. Mater. **206**, 287 (1993).

[86] B. H. Sencer, G. M. Bond, M. L. Hamilton, F. A. Garner, S. A. Maloy, and W. F. Sommer, Microstructural origins of radiation-induced changes in mechanical properties of 316 L and 304 L austenitic stainless steels irradiated with mixed spectra of high-energy protons and spallation neutrons, J. Nucl. Mater. **296**, 112 (2001).

[87] D. Chen, K. Murakami, K. Dohi, K. Nishida, Z. Li, and N. Sekimura, The effects of loop size on the unfaulting of Frank loops in heavy ion irradiation, J. Nucl. Mater. **529**, 151942 (2020).

[88] N. Hashimoto, E. Wakai, and J. P. Robertson, Relationship between hardening and damage structure in austenitic stainless steel 316LN irradiated at low temperature in the HFIR, J. Nucl. Mater. **273**, 95 (1999).

[89] D. S. Aidhy, C. Lu, K. Jin, H. Bei, Y. Zhang, L. Wang, and W. J. Weber, Point defect evolution in Ni, NiFe and NiCr alloys from atomistic simulations and irradiation experiments, Acta Mater. **99**, 69 (2015).